

# Nanoscale

Accepted Manuscript



This is an *Accepted Manuscript*, which has been through the Royal Society of Chemistry peer review process and has been accepted for publication.

*Accepted Manuscripts* are published online shortly after acceptance, before technical editing, formatting and proof reading. Using this free service, authors can make their results available to the community, in citable form, before we publish the edited article. We will replace this *Accepted Manuscript* with the edited and formatted *Advance Article* as soon as it is available.

You can find more information about *Accepted Manuscripts* in the [Information for Authors](#).

Please note that technical editing may introduce minor changes to the text and/or graphics, which may alter content. The journal's standard [Terms & Conditions](#) and the [Ethical guidelines](#) still apply. In no event shall the Royal Society of Chemistry be held responsible for any errors or omissions in this *Accepted Manuscript* or any consequences arising from the use of any information it contains.

# Kinetic Trapping through Coalescence and the Formation of Patterned Ag-Cu Nanoparticles

Panagiotis Grammatikopoulos<sup>†</sup>, Joseph Kioseoglou<sup>‡</sup>, Antony Galea<sup>†</sup>, Jerome Vernieres<sup>†</sup>, Maria Benelmekki<sup>†</sup>, Rosa E. Diaz<sup>†</sup>, Mukhles Sowwan<sup>†,||</sup>

<sup>†</sup>Nanoparticles by Design Unit, Okinawa Institute of Science and Technology Graduate University, 1919-1 Tancha, Onna-Son, Okinawa, 904-0495, Japan

<sup>‡</sup>Department of Physics, Aristotle University of Thessaloniki, GR-54124 Thessaloniki, Greece

<sup>||</sup>Nanotechnology Research Laboratory, Al-Quds University, East Jerusalem, P.O. Box 51000, Palestine

## Abstract:

During recent years, due to its inherent flexibility, magnetron-sputtering has been widely used to synthesise bi-metallic nanoparticles (NPs) via subsequent inert-gas cooling and gas-phase condensation of the sputtered atomic vapour. Utilising two separate sputter targets allows for good control over composition. Simultaneously, it involves fast kinetics and non-equilibrium processes, which can trap the nascent NPs into metastable configurations. In this study, we observed such configurations in immiscible, bi-metallic Ag-Cu NPs by scanning transmission electron microscopy (S/TEM) and electron energy-loss spectroscopy (EELS), and noticed a marked difference in shape of NPs belonging to Ag- and Cu-rich samples. We explained the formation of Janus or Ag@Cu core/shell metastable structures on the grounds of in-flight mixed NP coalescence. We utilised molecular dynamics (MD) and Monte Carlo (MC) computer simulations to demonstrate that such configurations cannot occur as a result of nanoalloy segregation. Instead, sintering at relatively low temperatures can give birth to metastable structures, which eventually can be stabilised by subsequent quenching. Furthermore, we compared the heteroepitaxial diffusivities along various surfaces of both Ag and Cu NPs, and emphasised the differences between the sintering mechanisms of Ag- and Cu-rich NP compositions: small Cu NPs deform as coherent objects on large Ag NPs, whereas small Ag NPs dissolve onto large Cu NPs, with their atoms diffusing along specific directions. Taking advantage of this observation, we propose controlled NP coalescence as a method to engineer mixed NPs of a unique, patterned core@partial-shell structure, which we refer to as “glass-float” (*ukidama*) structure.

**KEYWORDS:** *bi-metallic nanoparticles; silver-copper nanoalloy; co-sputtering; core/shell-Janus, molecular dynamics*

## Introduction

Bi-metallic nanoparticles (NPs) have recently attracted increasing interest, since, in addition to the tunable parameters of size, crystallinity and morphology of their single-component counterparts, they afford the possibility of combining different classes of physical properties by suitable selection of their constituents, making new and exciting applications possible for the first time.<sup>1-3</sup> For example, binary nanoalloys composed of a ferromagnetic and a plasmonic metal, such as AgCo, AuCo or AgNi NPs, demonstrate interesting magneto-optical properties for potential applications that depend on both their composition and structure.<sup>4,5</sup>

As a result, a great number of studies, both theoretical and experimental, were published over the last years with a focus on establishing the correlation between composition and structure for numerous bi-metallic NP systems, and on their effects on various physical properties, taking into account their component elements, fabrication method, size, etc.<sup>5-19</sup> A multitude of equilibrium atomic arrangements within NPs of specific geometric structures were determined, ranging from random or ordered solid solutions (for miscible systems) to core@shell, onion-type multi-shell, ball-and-cup, and Janus or quasi-Janus NPs (for immiscible systems). For a comprehensive discussion on the above, the interested reader is referred to ref. [20] and references therein. Various *ab initio*, atomistic, or global optimisation methods have been used in an attempt to identify the optimised chemical structures of binary nanoalloys<sup>21,22</sup> or construct nanophase diagrams.<sup>23-25</sup> However, due to either size-limitations inherent to the investigation methods, or due to size effects and various non-homogeneous conditions within each system, a complete quantitative structural description is still lacking for many systems, making the prediction of physical properties rather challenging.

Recent advances in gas-phase synthesis techniques<sup>19,26-28</sup> present liberating flexibility in fabricating bi-metallic NPs with tunable sizes, shapes and concentrations on the one hand, but, on the other hand, involve fast kinetics and non-equilibrium processes that often result in unpredictable metastable phases. However, approaching kinetic trapping phenomena as a challenge rather than as a hindrance, one can take advantage of the opportunity to design novel structures with unique properties.<sup>29-31</sup> To this end, there are three necessary prerequisites: (i) theoretical understanding of the physical processes involved during NP synthesis, (ii) experimental accurate size control and (iii) a method to stabilise the system into a desirable meta-stable configuration post-growth, to avoid restructuring due to ageing.<sup>32,33</sup>

This work deals mainly with the former point. We chose to study Ag-Cu bi-metallic NPs because it is a well-known immiscible system whose stable states have already been determined.<sup>5,23,34,35</sup> It is interesting not only because of the properties of the individual constituents that render it suitable for numerous applications (plasmonics, catalysis, bio-compatibility, etc.), but also because of their relative availability and low price.<sup>5,7</sup> We will show that a number of metastable NP configurations can be grown through a coalescence procedure. Coalescence of single-element NPs has been studied a lot in the past, both by the authors<sup>36-38</sup> and others.<sup>39-44</sup> Mixed-element studies are rarer and more complicated, but reported literature exists for the Ag-Cu system.<sup>45,46</sup> However, Mariscal *et al.* studied very small nanoclusters only (1.3 nm in diameter), whereas Chandross studied only equal-size Ag and Cu NPs and extrapolated his results for coalescence between NPs of different sizes, an approach that can be tricky due to the size-dependence of NP melting points.<sup>36</sup>

Coalescence is usually associated with surface diffusion. Therefore, another decisive factor for the resultant configurations is heteroepitaxial diffusion of adatoms of species A on surfaces of species B. For NPs, due to the simultaneous existence of facets of different orientations, the final configuration cannot be dictated by energetics alone; kinetics plays a more prominent role.<sup>6</sup> This means that it is also ambivalent to extrapolate conclusions drawn for 2D problems, where no alternative diffusion paths coexist. Finally, although we do not focus on points (ii) and (iii) in this work, recent literature indicates that both accurate NP size control and post-growth stabilisation can be achieved via multi-target sputtering<sup>27,47,48</sup> and embedding in suitable matrices, polymer spin-coating etc.<sup>49,50</sup>, respectively, opening up opportunities for sophisticated bi-metallic NP design.

## Method

### Experiment

Silver and Copper NPs were synthesised by gas-aggregation sputter deposition (Nanogen-Trio source, Mantis Deposition Ltd., UK), as reported by Haberland *et al.*<sup>51</sup>, onto undoped Si dice ( $10 \times 10$  mm), and  $\text{Si}_3\text{N}_4$  TEM grids. The water-cooled aggregation chamber was evacuated down to  $10^{-6}$  mbar prior to sputtering. High-purity Cu (99.99%) and Ag (99.99%) targets were used separately in a DC co-sputtering process. Constant pressure was maintained at  $3 \times 10^{-1}$  mbar in the aggregation zone and  $7.5 \times 10^{-4}$  mbar in the main chamber with constant argon (Ar) flow rate set at 80 sccm. Keeping the other parameters constant, fine-tuning of the DC power ensures good control over the average composition of the different samples, due to the differences between the two species in atomic mass (Cu: 63.54 amu and Ag: 107.86 amu) and sputtering yield (Cu: 1.12 at 246 eV and Ag: 1.39 at 215 eV).

Post-deposition *ex-situ* x-ray photoelectron spectroscopy (XPS; Axis UltraDLD, Kratos Analytical Ltd., UK) was performed on samples deposited on Si substrates to quantify the average composition of the bi-metallic nanomaterials. The size and morphology of these NPs were examined using an image-corrected scanning/transmission electron microscope (S/TEM) FEI Titan 80-300 kV operated at 300 kV. Energy electron-loss spectroscopy (EELS) was used to study individual NP composition by chemical mapping of each species. All TEM samples were transferred inside a vacuum transfer holder and TEM experiments were performed under vacuum to avoid any oxidation due to air exposure.

### Computer Simulation

Molecular dynamics (MD) calculations were performed with the LAMMPS MD simulator<sup>52</sup>, utilising an embedded-atom method (EAM) interatomic potential that reproduces accurately the entire Cu-Ag phase diagram, in good agreement with experiment.<sup>53</sup> Three different sets of MD simulations were run; the rationale behind their choices will be elaborated in the results section. First, demixing of alloy NPs of various diameters (3, 5, 7 and 9 nm, containing 887, 3925, 10641 and 22543 atoms, respectively) and compositions (20, 35, 70, 90 at.% Cu) was investigated at various temperatures below their estimated melting point (700-1000 K). Initially, Cu atoms randomly substituted Ag atoms in a Ag fcc matrix. The investigation of Cu segregation was performed under the canonical NVT ensemble utilising a Nosé-Hoover thermostat.<sup>54,55</sup> Then, prior to performing coalescence studies, the melting temperatures of single-element Cu and Ag NPs in the size regime of interest (i.e. 3, 5, 7, and 9 nm in diameter) were calculated more accurately by plotting caloric curves for single NPs. Each NP

was equilibrated at discrete temperature intervals and its potential energy vs. temperature graph was drawn; a steep increase in potential energy, associated with a sudden release of heat of fusion, marks the onset of melting. Finally, the coalescence between NPs of different species (Ag or Cu) was simulated. Several configurations were investigated, with NP sizes of either species ranging between 3-9 nm. First, the NPs (which were initially near-spherical objects cut from a bulk structure) were relaxed individually at various temperatures (500-1200 K) using the NVT ensemble, and subsequently they were inserted in the same simulation box in a distance just short of the cut-off radius of the interatomic potential<sup>53</sup>, and their coalescence was investigated using the microcanonical NVE ensemble, to allow for their heating due to surface energy annihilation.

For our demixing studies, MD simulations were also complemented by Monte Carlo (MC) simulation runs in order to sample the potential energy landscape more efficiently and find the equilibrium structures of the NPs. A MC-based swap of atoms following the Metropolis algorithm was implemented after short sequences of 5 MD steps in the canonical ensemble, where the MD temperature was also used in the Metropolis criterion dictating the swap probability. MC simulations were up to  $\sim 4 \times 10^6$  steps long. The final configuration of this combined method can be regarded as the result of a longer, pure MD simulation in the NVT ensemble.

## Results and Discussion

Bi-metallic AgCu NPs were synthesised using a magnetron-sputtering system<sup>13,14,27,56</sup>, as schematically illustrated in Fig. 1. Utilising two independent, pure-element sputter targets means that single-species nascent nanoclusters were initially formed inside their respective plasma zones, only to coalesce into larger mixed NPs later on in the comparatively colder aggregation zone. This technique enabled the deposition of samples with a broad spectrum of relative compositions. Keeping all other deposition parameters constant, the abundance ratios of Ag to Cu were solely determined by the DC power applied to their respective targets.

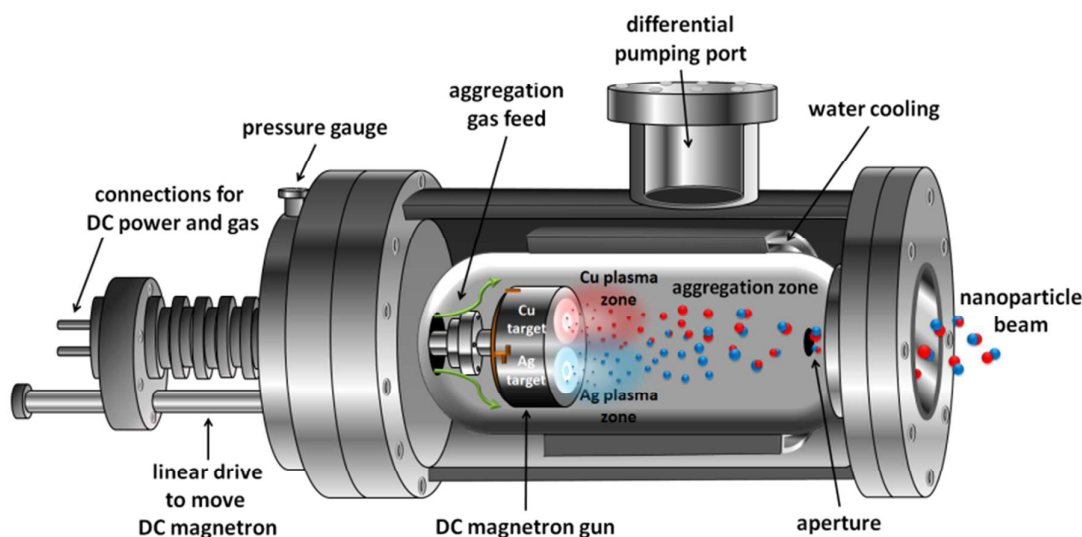


Fig. 1 Schematic representation of a modified magnetron-sputtering inert-gas condensation system utilising a dual target configuration.

This was confirmed by post-deposition *ex-situ* XPS analysis, performed to determine the elemental quantification of each species within a wide scan area (the x-ray spot size of  $3 \times 7 \mu\text{m}$  covers an area subsequently determined to enclose approximately 20000 particles). As evident from the XPS data and the relatively simple analytical form of their fitting curve (Fig. 2), a good control over the composition of the deposits was thus achieved. For simplicity, in what follows we will focus only on two of the obtained samples with near-symmetrical compositions: the 68 at.% Cu one (henceforth Cu-rich sample) and the 65 at.% Ag one (henceforth Ag-rich sample). They were obtained keeping the power of the Cu target constant (20 W) and changing the power of the Ag target from 10 to 20 W, respectively.

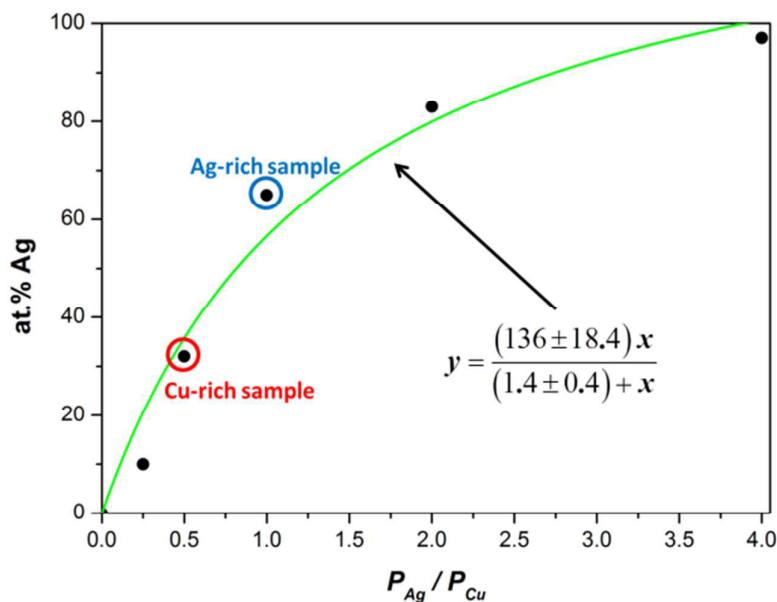


Fig. 2 Relative elemental compositions of depositions correlate directly with DC powers of independent sputter targets.

Exemplary dark field S/TEM images at 300 kV of the Ag-rich and Cu-rich samples are depicted in Figs. 3(a) and (b), respectively, showing similar, relatively low coverage. Several such micrographs per sample under the same conditions were used to obtain particle lateral size distributions, shown in the inset of Fig. 3(c). It is worth noting that mass filtration was not used for this study; therefore, both size distributions are relatively wide, with peaks at 8.19 and 14.92 nm and full-width at half-maximum values of 10.7 and 20.5 nm for the Ag-rich and Cu-rich samples, respectively. There is, however, a striking difference in shape between the size distributions of the two samples: the Cu-rich one presents both a markedly lower peak and a greater size dispersion. The high and narrow shape of the Ag-rich distribution is a result of Ag forming a large number of smaller-size nanoclusters compared to Cu, due to its lower evaporation temperature.<sup>6</sup> Since the same sputtering conditions were used for Cu in both samples, one would expect larger mixed NPs to form in the sample where more Ag was sputtered, i.e. the Ag-rich sample. However, this is clearly not the case in the distributions of Fig. 3. The reason for this discrepancy lies in the implicit assumption during the calculation of the S/TEM size distributions that the NPs are of spherical shape, which mistakes what are actually the lateral sizes of oblong, partly-coalesced clusters or irregular agglomerates for diameters of spherical NPs. This clarification (which is verified when explicitly identifying each entity

considered to be a single NP, e.g. see Supplementary Material Fig. S1 for the Ag-rich sample) also explains the unexpectedly large nominal size of the NPs. At the same time, it implies that the tendency of NPs to coalesce or form agglomerates is different between the Ag- and Cu-rich samples.

In order to scrutinise this irregularity in the behaviour of the two samples, a particle counting script (Digital Micrograph) with a carefully adjusted threshold was employed to measure the area and perimeter of each particle. Under the tentative assumption that all particles had circular projections, two radii values,  $R_a$  and  $R_p$ , were subsequently calculated and assigned to them, for each area and perimeter value, respectively. In the case of spherical particles,  $R_a$  and  $R_p$  values coincided, whereas for asymmetrical particles, these values diverged. Despite some uncertainty inherent to this method, self-consistency in the mode of measurement was expected to reveal, at least qualitatively, any dominant trends. Fig. 3(c) contains a scatter plot of  $R_a$  vs.  $R_p$  values, and, indeed, such an inescapable tendency is evident. NPs of the Cu-rich sample deviate a lot more from the line that indicates a circular projection (thus, implying a spherical shape) than their Ag-rich counterparts. Clearly, an irregular shape is more probable for NPs of the Cu-rich sample.

As mentioned above, two possible mechanisms were put forward to account for this trend: (i) variation between the two samples in the degree of nanocluster coalescence in-flight during NP growth and, (ii) variation in the degree of NP agglomeration after landing on the substrate. Indeed, both mechanisms influence the shape of the NPs of Figs 3(a) and (b); however, the size-domains where each mechanism is dominant differ. Nanocluster coalescence dominates deviations from a spherical shape in the small-size regime, and accounts for the positions of the peaks of the size distributions. Subsequent NP agglomeration is more important for larger particle sizes, expediting further deviations and thus creating Y-shaped forks in the scatter plots; NP agglomeration accounts for the log-normal tails of the size distributions. The two branches for each scatter plot are indicated in Fig. 3(c) by the letters “c” (for coalescence dominance) and “a” (for agglomeration dominance). There is inherent randomness in the agglomeration mechanism, which stems from the random nature of the deposition, especially considering the low coverage and the fact that the substrates were kept at room temperature thus suppressing post-deposition surface diffusion; indeed, the scatter points of the “a” branches overlap considerably. In the small-size regime, on the other hand, there is a clear inclination for NPs of the Ag-rich sample to appear more spherical, indicating a tendency for fuller coalescence upon growth.

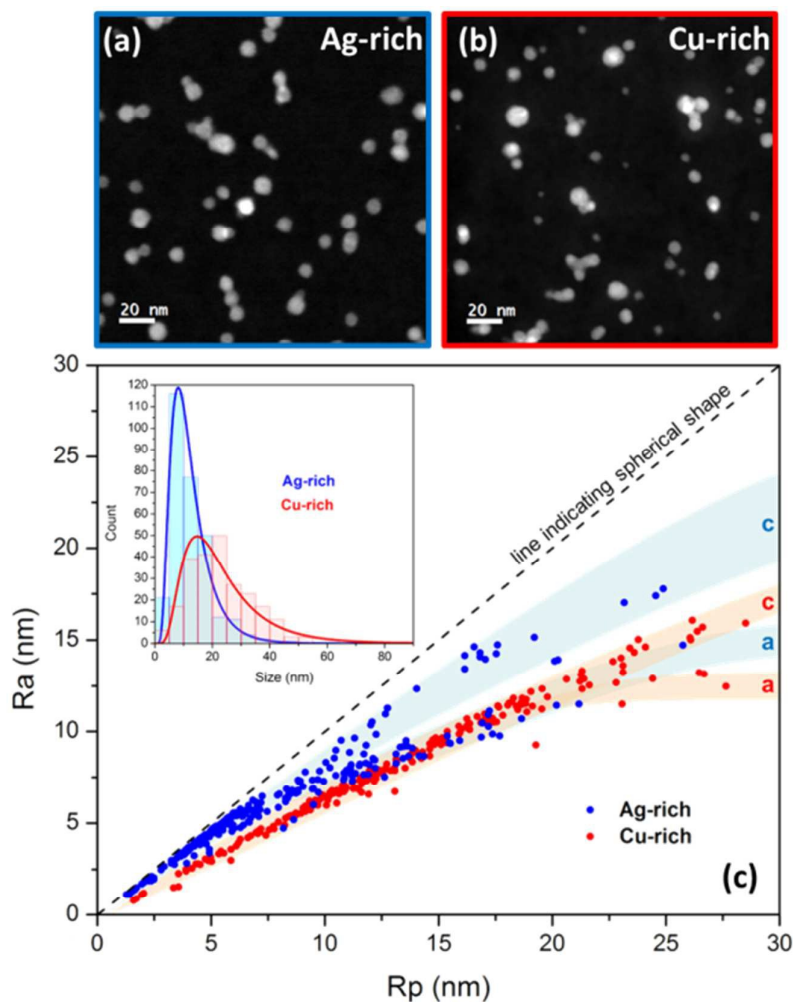


Fig. 3  $193 \times 193$  nm dark field STEM micrographs of Ag-rich (a) and Cu-rich (b) samples. (c) Scatter plot of radii values obtained from NP perimeter vs. area. Different deviation trends are observed for the two samples (accentuated by blue and red underline colours), implying more irregular shapes for Cu-rich particles. The size distributions of both samples are shown in the inset.

Nevertheless, to reach a conclusion based on these data alone would be hasty, since the accuracy of our measurement method could, in principle, vary with NP size. To understand the origin of this dissimilarity between the two samples, EELS elemental maps were obtained. A variety of morphological classes were observed, including pure Ag or Cu NPs, Ag-Cu Janus particles, and partial or full Ag@Cu and Cu@Ag core/shell particles. An exemplary collection of specimens from such classes is shown in the first row of Figs 4(a)-(e); their content in Ag increases from an almost pure-Cu Cu@Ag NP in (a) through a Ag-rich dumbbell in (c) to an almost pure-Ag Ag@Cu NP in (e). In the following two rows, the NPs are decomposed according to element. Extended analysis using EELS point scan measurements within a representative NP (Fig. 4(b)) are shown in Fig. 4(f). The presence of a Cu edge ( $\text{Cu-L}_{2,1}$ ) and Ag peak ( $\text{Ag-M}_{4,5}$ ) are clearly evident from areas 1 and 2, which correspond to the core and the shell of the NP, respectively. An additional peak from the TEM grid ( $\text{Si}_3\text{N}_4$ ) is revealed on area 3, corresponding to the nitride peak. It is evident from the EELS analysis that no sign of oxidation was present in our samples.

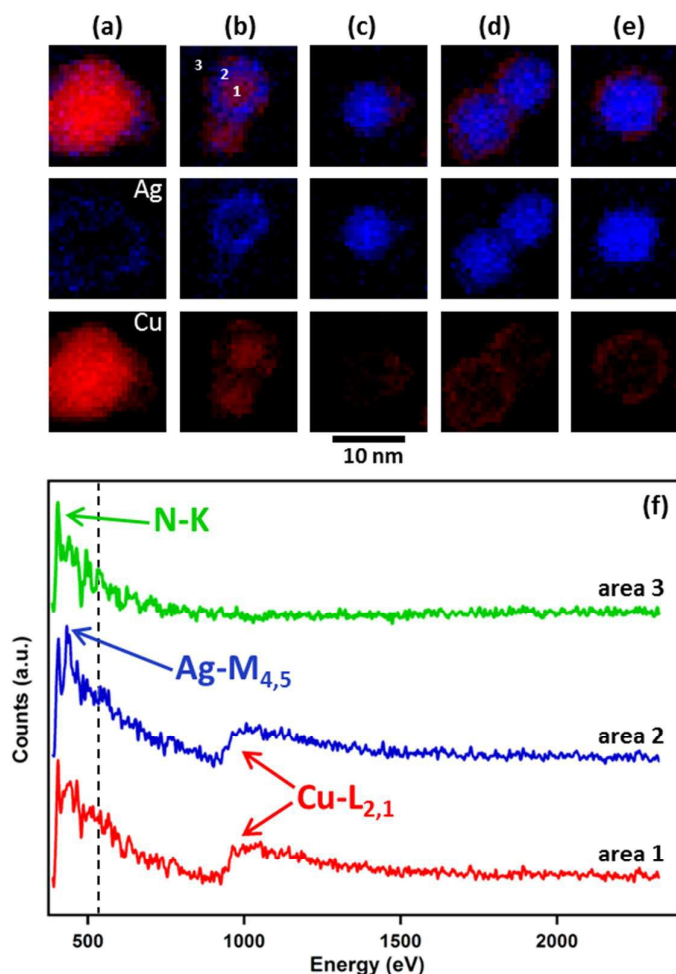


Fig. 4 (a)-(e) Exemplary collection of EELS elemental maps demonstrating various morphologies with increasing Ag content (first row). In the next rows, the particles are decomposed according to element (second row: Ag, third row: Cu). (f) EELS spectra of a representative NP (b) showing that the core is composed mainly of Cu and the shell is composed of Ag. No sign of oxidation was present in these spectra (black dotted line).

The most striking feature of the EELS maps in Fig. 4 is the presence of structures with Cu on the surface (either Janus or Ag@Cu core/shell NPs). It is well established in literature that the Ag-Cu system is a highly immiscible one, with a positive enthalpy of mixing providing the driving force for phase segregation.<sup>35,57</sup> Both the atomic sizes and surface energies of Ag and Cu<sup>46</sup> are such that a Cu-core/Ag-shell configuration is energetically favourable and, therefore, most expected; as a rule of thumb, lower surface energy coats higher surface energy, and small atom species occupies core positions with large atom species forming a shell to relieve strain. Indeed, a great number of studies, both theoretical and experimental verified this fact.<sup>5,23,34,35,58</sup> Therefore, configurations such as those in Figs 4(c)-(e) are metastable and cannot be explained purely from an energetics point of view.

Once more, the explanation behind the formation of these unfavourable structures lies in the gas-phase synthesis method of these NPs, which involves fast kinetics and non-equilibrium processes. Utilising two separate sputter targets instead of an alloy target resulted in independent nucleation

and growth of nascent nanoclusters of each species, which subsequently coalesced with each other, producing mixed NPs of the configurations shown in Fig. 4. Had the nanoclusters grown together in a mixed-species plasma zone, nascent liquid nanoalloys would have been formed, which, upon solidification, would have segregated in an energetically favourable fashion, i.e. with Ag atoms migrating to the surface, as all global optimisation studies suggest.<sup>34</sup>

To put this postulate to the test, MD simulations were employed in order to elucidate the formation mechanism of the metastable configurations of Fig. 4. First, elemental surface segregation was studied. It is known that phase separation depends on NP size; under a threshold size, specific for each system, variations in atomic sizes and surface energies are not pronounced enough to trigger segregation.<sup>35</sup> Therefore, nanoalloy systems of various diameters, ranging between 3 and 9 nm, were constructed. To produce MD results directly comparable to experimental data, random solid solutions were chosen with 70 at.% Cu (Cu-rich) and 65 at.% Ag (Ag-rich). Each NP size was annealed to high temperatures, but well beneath its melting point. Clear separation tendencies were observed at all cases, with Ag atoms always segregating to the surface and forming shells of a single atomic layer thickness. Figs. 5(a-b) show the initial and final configurations for Cu- and Ag-rich NPs, 3 nm in diameter, after annealing at 700 K for 70 ns, whereas Figs. 5(c-d) show the corresponding final configurations of NPs 5 nm in diameter, maintaining better their initial monocrystalline structure. Regardless of NP size, in the Cu-rich cases this process led to the formation of Cu@Ag core/shell structures. In the Ag-rich cases Cu precipitates were formed, which moved to sub-surface positions, eventually leading to onion-type multi-shell structures (i.e. Ag@Cu@Ag). Practically identical results were obtained by a combined MD-MC method corresponding to prolonged MD simulation runs, as shown in Supplementary Material Fig. S2. Both structure types have been reported to be energetically favourable<sup>20</sup> and are clearly indicated by the atomic population histograms at the bottom of Figs. 5(a-b). No metastable or oblong configurations can be generated through a demixing mechanism. Thus, surface segregation was ruled out as a potential mechanism that could generate structures such as those of Fig. 4.

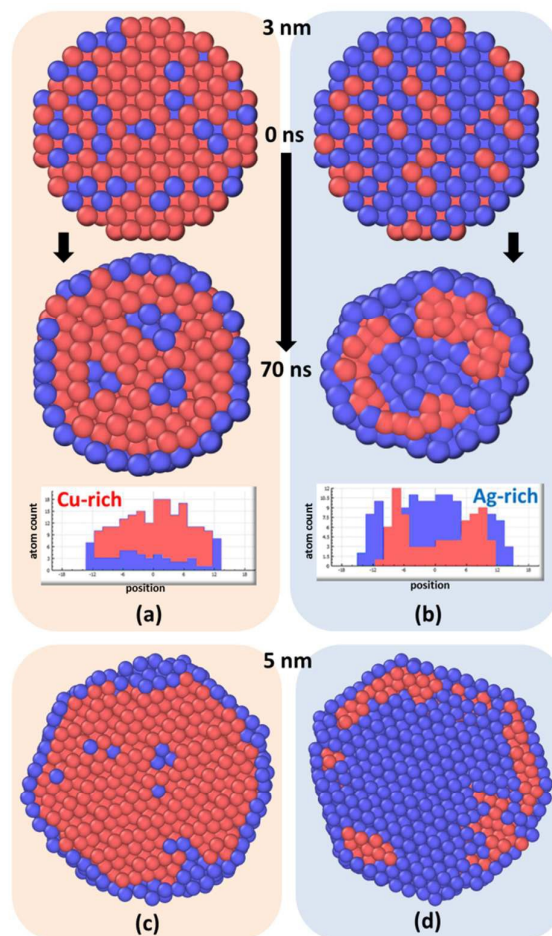


**Fig. 5** Cross-section of Cu-rich (a) and Ag-rich (b) nanoparticles, 3 nm in diameter, before and after annealing at 700 K for 70 ns. Red and blue spheres represent Cu and Ag atoms, respectively. A clear tendency for formation of Cu@Ag core/shell structure is observed in the Cu-rich case, whereas a Ag@Cu@Ag onion-type structure emerges in the Ag-rich shape. The histograms in the bottom of both figures show the populations of each atomic species across the equatorial plane of the particles, verifying these structures. In (c) and (d), the corresponding final configurations of NPs 5 nm in diameter reveal identical ordering as their 3 nm counterparts, while still maintaining their monocrystalline structure. NP sizes are not to scale.

Consequently, NP coalescence was tested to verify whether it could reproduce the metastable configurations of Fig. 4. Before conducting any sintering simulations, it is imperative to calculate the melting temperatures of NPs as a function of their size. According to our previously reported expanded cluster heating model of NP coalescence, the difference between the current temperature and the melting points of sintering NPs of any given size is the most important factor that dictates the degree of coalescence and defines the temperature regimes of full fusion or partial wetting of one NP onto another.<sup>36</sup> Caloric curves for single Ag and Cu NPs 3-9 nm in diameter are shown in Fig. 6; the points of discontinuity in the potential energy vs. temperature graph are a result of the latent heat of fusion released upon melting, and the corresponding temperatures are the melting temperatures. As expected from their bulk counterparts, Ag NPs of all sizes have consistently lower

melting points than Cu NPs of the same size (980, 1120, 1170, 1190 ( $\pm 10$ K) and 1020, 1170, 1220, 1250 ( $\pm 10$ K) for Ag and Cu NPs 3, 5, 7 and 9 nm in diameter, respectively).

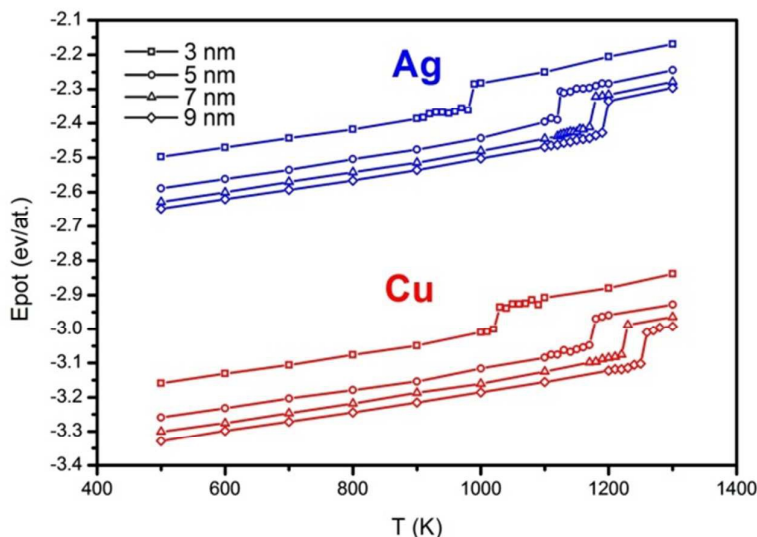


Fig. 6 Temperature dependence of potential energy for single Ag and Cu NPs, 3, 5, 7 and 9 nm in diameter. Slope changes indicate melting points.

Once the melting points of all NP sizes of interest (3-9 nm) had been determined, coalescence between NPs of different species (Ag or Cu) was simulated. During experimental growth, the Ag and Cu NPs were mixed in the aggregation zone, which is estimated to be at around room temperature. However, since coalescence is a process that incorporates atomic diffusion, it is assisted by higher temperature; therefore, we ran simulations at rather exaggerated temperatures to speed up the sintering of the nanoclusters. Having calculated the melting points in advance enabled us to avoid overheating that could lead to melting and simulation artefacts. The final configurations after 180 ns of MD runs of pairs of NPs sintering at 600 K (well below the melting points of either species at all sizes) are shown in Fig. 7. Sintering of NPs 3 and 7 nm in diameter of both combinations correspond to the experimental Ag- and Cu-rich samples, as indicated in the figure, since the resultant configurations contain 30% Cu or Ag, respectively. The red dotted line indicates a rough estimate of relative Ag and Cu NP sizes with equal melting temperatures, such as the one depicted in the figure: both 7 nm Ag and 5 nm Cu NPs were found to melt at 1170 K. Also included in the figure are the 3-9 nm combinations, since they were expected to showcase any occurring phenomena more clearly.

Detailed descriptions of the coalescence mechanisms and associated phenomena have been reported before.<sup>37-43</sup> In a nutshell, heat released due to free-surface annihilation is absorbed by the NPs and temporarily enhances surface pre-melting. Necking, thus, occurs, with neck sizes depending on how many bonds of the surface atoms break initially; in principle, this depends on the current temperature-to-melting point ratio. Put differently, full or partial wetting of the NP with the lowest melting point occurs onto the NP with the highest melting point.<sup>37</sup> The extent of this wetting determines the resultant sphericity of the sintered binary NP. Therefore, it would be reasonable to assume that configurations containing small Ag NPs would lead to enhanced coalescence (and, therefore, more spherical resultant structures), since Ag NPs have lower melting points. However, it is evident from Fig. 7 that this is not the case: under the same circumstances, Ag-rich configurations

experience faster or more pronounced coalescence than their Cu-rich counterparts, rather counter-intuitively but in full agreement with our experimental result of Fig. 3.

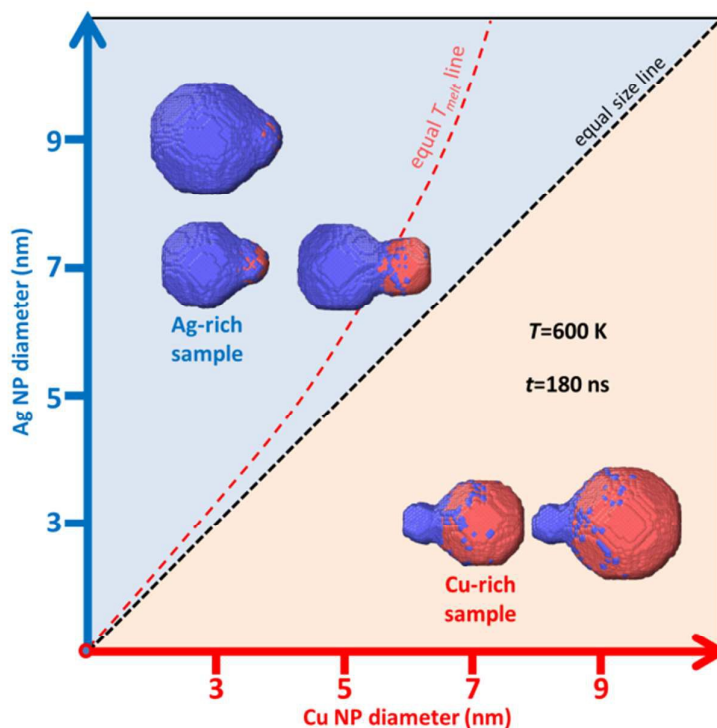


Fig. 7 Final configurations after 180 ns of MD runs of pairs of NPs sintering at 600 K.

The explanation to this seemingly unexpected observation lies in the inherent differences in physical properties between the two atomic species involved. To begin with, due to its lower surface energy (on average  $\sim 0.15$  eV/atom lower than that of Cu<sup>59</sup>), Ag always has the tendency to move to the surface, no matter what the composition of the sintered sample. In Cu-rich samples this means that the small Ag cluster partially wets the surface of the larger Cu cluster when it absorbs heat released through free surface annihilation. In Ag-rich samples it is the Cu cluster that melts partially; however, Ag atoms still migrate to the surface, creating a (complete or partial) monatomic outer shell. This leads to the formation of two interfaces instead of one, further increasing the temperature of the clusters.

Normally, this extra heating alone (of the order of a few tens of degrees K, depending on temperature) does not suffice to enhance coalescence in any noticeable way. However, in conjunction with the vast cohesive energy difference between the two species (0.69 or 0.83 eV/atom higher for Cu, according to different studies<sup>46,60</sup>), it results in two completely dissimilar coalescence mechanisms observed for the two samples: (i) in the Ag-rich sample, the small Cu cluster, assisted by the released heat, is flattened as a single, cohesive object, maximising its interfacial area with the large Ag cluster in order to reduce its overall potential energy.<sup>6,46</sup> (ii) In contrast, in the Cu-rich sample it is the atoms of the smaller Ag cluster which are adjacent to the interface that absorb the released heat and surface-diffuse on the large Cu cluster. Whereas the former mechanism involves a simultaneous process (i.e. flattening of Cu cluster), the latter is a

sequential process: the atoms leave the small Ag cluster in succession, emaciating it gradually. This is why Ag-rich samples exhibit higher degrees of coalescence (i.e. appear more spherical) at any given time. If the NPs are cooled down fast, they can be trapped in any current configuration such as those depicted in Fig. 7, explaining both the asymmetry in the coalescence behaviour of the two experimental samples shown in Fig. 3 and the metastable structures depicted in Fig. 4. Indeed, experimentally grown NPs do undergo quenching when they enter different compartments of the sputtering apparatus, such as, for example, the ultra-high vacuum deposition chamber. Naturally, if left to sinter for longer times at relatively high temperatures, both samples would lead to fully coalesced, spherical configurations, identical to those produced by the segregation process of Fig. 5. Such stable configurations are shown in Supplementary Material Fig. S3; once more, in this figure, higher temperatures compensate for relatively short simulation times.

The most important aspect regarding the formation of coalesced structures concerns the heteroepitaxial diffusivity on different facets of the larger cluster. As mentioned in the Method section, initially the NPs were near-spherical objects cut from a bulk structure, which were later relaxed individually. Because Ag and Cu crystals belong to the fcc system, both NP types relaxed towards near-truncated octahedron (TO) structures, displaying {100}, {110} and {111}-type facets and numerous steps along the edges between these facets.<sup>20,37</sup> It is worth noting that, due to the relatively large size of the NPs, the facets are not distorted, unlike previously reported work on much smaller Cu NPs.<sup>35</sup> The time evolution of the coalescence process at 800 K of systems comprising a 3 nm Ag and a 9 nm Cu NP is shown in Fig. 8(a-c). In each row, the small Ag NP is adjacent to a different facet of the large Cu NP (i.e. {100}, {110} and {111} for (a), (b) and (c), respectively). All simulations were run until full fusion of the two NPs was obtained and a stable configuration was reached. The process of coalescence through surface diffusion is more clearly shown in animations available in the Supplementary Material online (Supplementary Movies 1-3). It is evident that, regardless of the original position of the Ag NP, its atoms end up mainly on narrow {110} facets formed between wider {111} surfaces, or, secondarily, on {100} facets, consistently showing a strong tendency to avoid {111} facets. This is in good agreement with previously reported studies of adatom adsorption on various Cu facets using MD, or density functional theory based simulations in combination with the nudged elastic band method. Energetics calculations of the diffusion process for single Ag adatoms on Cu surfaces showed that diffusion is extremely fast on {111} facets, with barriers below 0.1 eV, but slower on {100} and {110} facets, with barriers  $\sim 0.3$  eV, preventing the adatoms from settling on {111} surfaces. For diffusion across intra-facet steps the barriers are much higher,  $\sim 0.7$  eV, whereas those for diffusion along step edges are low,  $\sim 0.2$  eV, indicating a preferential diffusion path along, rather than across, the step edges.<sup>35,61,62</sup>

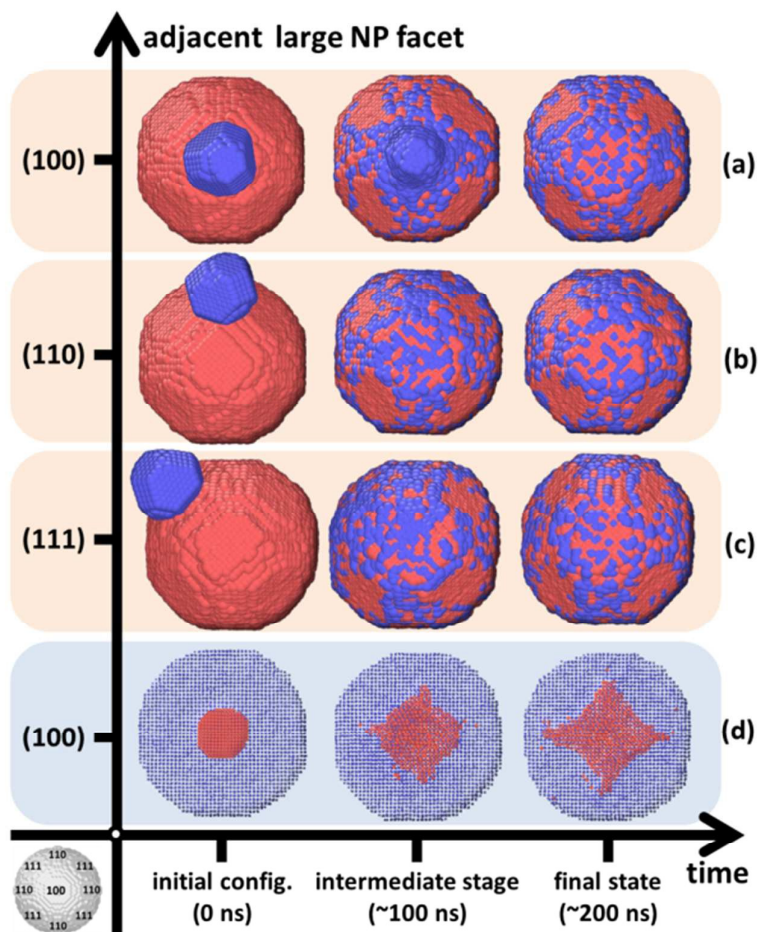


Fig. 8 Time evolution of the coalescence process at 800 K of systems comprising a 9 nm Cu NP and a 3 nm Ag NP adjacent to (100), (110) and (111) facets (a-c, respectively) and a 9 nm Ag NP with a 3 nm Cu NP adjacent to a (100) facet (d). At all cases, (111) facets remain clear of any heteroatomic deposition.

As a result, the NPs attained a patterned core@partial-shell configuration that had not been identified before. Indeed, Chandross did report the same diffusion path for Ag atoms on a Cu NP surface, but did not observe this specific pattern formation, since he only simulated NPs of the same size.<sup>46</sup> Lu *et al.*, on the other hand, observed this configuration during heating experiments by high-angle annular dark-field (HAADF) Z-contrast imaging<sup>63</sup>, and described it as an epitaxial Ag{111}/Cu{111} interface. However, an observation from a different angle that could bring the {111} facet in plan-view would reveal the deposition of the Ag atoms along intra-facet steps between (rather than on top of) Cu {111} facets, experimentally validating the MD simulation results that are supported by the diffusion theoretical analysis. Lu *et al.* explained their experimental observation based on the fact that this type of Ag-Cu interface has the lowest interfacial energy.<sup>64</sup> However, emphasis should be given to the difference between NPs and 2D surfaces: minimisation of interfacial energy and low diffusion barriers are of importance in order to interpret the 2D, smooth and flat epitaxial growth of films, but in the case of NPs, where various surfaces of different orientations coexist, preferential atomic diffusion can prevent the growth of specific interfaces. Langlois *et al.*<sup>6</sup>

describe the growth of Ag on Cu {111} following a layer-by-layer (Frank-van der Merwe) growth mode, which is consistent with the low diffusion barrier of Ag adatoms on this particular surface; simultaneously, they warn about the complexity that arises with such statements regarding NPs, due to the coexistence of facets of various orientations. In the case study presented here, the low diffusion barriers on specific surfaces (e.g. on Cu {111} facets) led to the fast migration of the Ag adatoms away from them, whereas the high diffusion barriers on other surfaces (e.g. on Cu {110} facets) led to their enclosure by the Ag atoms, as elucidated by the MD simulations and illustrated in Fig. 8 and Supplementary Movies 1-3.

It should be stressed that this structure is not the same as the ball-and-cup configuration that has been reported in the past (refs. 22,65), where a Cu core is half-covered by a monolayer of Ag. Instead, the configurations of Fig. 8 consist of spherical Cu cores enclosed by external “cages” of Ag atoms, resembling Japanese glass-floats (locally known as *ukidama*), where spherical glass buoys are surrounded by fishnet ropes. A similar structure has been reported as the equilibrium structure of Co-rich CuCo alloy NPs, when the amount of Cu does not suffice to form a complete shell, since the energy gain from a Cu atom substituting Co atoms in {100} facets is larger than in {111} ones.<sup>18</sup> From an engineering point of view, the potential importance of designing such structures is self-evident, since they may be fine-tuned to present unique optical properties or coated with another low surface energy species to create alternating interfaces, e.g. for plasmonics applications, or hollowed out by etching out the Cu core for drug delivery or catalysis applications, etc.<sup>66</sup>

Finally, time evolution of the coalescence process at 800 K of the reverse structure, i.e. a 9 nm Cu Ag and a 3 nm Cu NP adjacent to the (100) surface is shown in Fig. 8(d). Due to the presence of Ag atoms on the surface of the Cu NP, to enable the Cu atoms to be visible, atoms are depicted smaller than for the Cu-rich cases above. Evidently, diffusion of Cu on Ag is much more difficult for various reasons. First, as mentioned above, Cu-Cu bonds are stronger than Ag-Ag ones (~0.7 eV higher binding energy), meaning that Cu atoms are more prone to form cohesive clusters. Moreover, there is a relatively high diffusion barrier (e.g. ~0.6 eV and ~0.7 eV for the {100} and {111} Ag facets, respectively) due to the lattice mismatch and the diffusion mode of Cu monomers on Ag.<sup>60,62</sup> The reduced diffusivity of Cu on Ag may be due to the effect of the tensile strain of the Ag lattice.<sup>61</sup> Despite the differences with the Cu-rich sample, once again it is evident that Cu atoms avoid the {111} facets of the Ag NP, with the Cu NP expanding along {110} facets.

## Conclusions

Bi-metallic Ag-Cu NPs were synthesised by dual-target magnetron-sputtering via subsequent inert-gas cooling and gas-phase condensation, and were characterised by STEM and EELS. Due to the fabrication method that involved in-flight sintering of single-species nanoclusters, a highly non-equilibrium process, a great number of resultant configurations were detected, including various metastable ones, such as Janus or Ag@Cu core/shell NPs. Kinetic trapping effects are not uncommon in nanoalloys, due to simultaneous interplay of different degrees of freedom such as size and composition.

Utilising atomistic MD simulations, the following conclusions were drawn: (i) Starting from a random nanoalloy configuration, elemental segregation occurs towards energetically favourable directions, with Ag atoms always moving to the surface of the NPs. In the cases studied here, this resulted in the formation of Cu@Ag core/shell structures for Cu-rich NPs, and onion-type Ag@Cu@Ag multi-shell

structures for Ag-rich NPs, which were the expected structures based on previous literature. (ii) Coalescence well below the melting point of the NPs can produce metastable configurations. Interestingly, the coalescence mechanisms differ according to the relative sizes of the sintering NPs: small Cu NPs deform as coherent objects on large Ag NPs, whereas small Ag NPs dissolve onto large Cu NPs, with their atoms diffusing along specific directions. (iii) Even at higher temperatures, kinetics, rather than energetics, play a dominant role in adatoms which leave the Ag NP being deposited on specific facets on the large Cu NP (i.e. principally along intra-facet steps of {110} orientation). This is dictated by the simultaneous co-existence in a NP of free surfaces of various orientations with different adatom diffusion coefficients. (iv) Because of this preferential deposition, a Cu@Ag patterned core@partial-shell structure was observed, which we refer to as “glass-float” (*ukidama*) structure, with potential for various technological applications.

### Acknowledgment

This work was supported by funding from the Okinawa Institute of Science and Technology Graduate University. The authors would like to thank Stephan Steinhauer for useful discussion and advice.

### References

- 1 E. Ringe, J. M. McMahon, K. Sohn, C. Cobley, Y. N. Xia, J. X. Huang, G. C. Schatz, L. D. Marks and R. P. Van Duyne, *J. Phys. Chem. C*, 2010, **114**, 12511-12516.
- 2 R. Ferrando, J. Jellinek and R. L. Johnston, *Chem. Rev.*, 2008, **108**, 845-915.
- 3 Z. Y. Li, J. P. Wilcoxon, F. Yin, Y. Chen, R. E. Palmer and R. L. Johnston, *Faraday Discuss.*, 2008, **138**, 363-373.
- 4 M. Gaudry, E. Cottancin, M. Pellarin, J. Lermé, L. Arnaud, J. R. Huntzinger, J. L. Vialle, M. Broyer, J. L. Rousset, M. Treilleux and P. Mélinon, *Phys. Rev. B*, 2003, **67**, 155409.
- 5 D. Bochicchio and R. Ferrando, *Phys. Rev. B*, 2013, **87**, 165435.
- 6 C. Langlois, Z. L. Li, J. Yuan, D. Alloyeau, J. Nelayah, D. Bochicchio, R. Ferrando and C. Ricolleau, *Nanoscale*, 2012, **4**, 3381-3388.
- 7 K. Laasonen, E. Panizon, D. Bochicchio and R. Ferrando, *J. Phys. Chem. C*, 2013, **117**, 26405-26413.
- 8 G. Rossi, R. Ferrando and C. Mottet, *Faraday Discuss.*, 2008, **138**, 193-210.
- 9 D. Pohl, U. Wiesenhütter, E. Mohn, L. Schulz and B. Rellinghaus, *Nano Lett.*, 2014, **14**, 1776-1784.
- 10 F. Yin, Z. W. Wang and R. E. Palmer, *J. Am. Chem. Soc.*, 2011, **133**, 10325-10327.
- 11 R. Esparza, O. Téllez-Vázquez, G. Rodríguez-Ortiz, A. Ángeles-Pasqual, S. Velumani and R. Pérez, *J. Phys. Chem. C*, 2014, **118**, 22383-22388.
- 12 M. Bohra, P. Grammatikopoulos, R. E. Diaz, V. Singh, J. Zhao, J.-F. Bobo, A. Kuronen, F. Djurabekova, K. Nordlund and M. Sowwan, *Chem. Mater.*, 2015, **27**, 3216-3225.
- 13 J. Vernieres, M. Benelmekki, J.-H. Kim, P. Grammatikopoulos, J.-F. Bobo, R. E. Diaz and M. Sowwan, *APL Mater.*, 2014, **2**, 116105.

- 14 V. Singh, C. Cassidy, P. Grammatikopoulos, F. Djurabekova, K. Nordlund and M. Sowwan, *J. Phys. Chem. C*, 2014, **118**, 13869-13875.
- 15 C. Cassidy, V. Singh, P. Grammatikopoulos, F. Djurabekova, K. Nordlund and M. Sowwan, *Sci. Rep.*, 2013, **3**, 3083.
- 16 M. Hennes, J. Buchwald, U. Ross, A. Lotnyk and S. G. Mayr, *Phys. Rev. B*, 2015, **91**, 245401.
- 17 Y. Wang and M. Hou, *J. Phys. Chem. C*, 2012, **116**, 10814-10818.
- 18 A. A. Dzhurakhalov and M. Hou, *Phys. Rev. B*, 2007, **76**, 045429.
- 19 D. Llamasa, M. Ruano, L. Martínez, A. Mayoral, E. Roman, M. García-Hernández and Y. Huttel, *Nanoscale*, 2014, **6**, 13483.
- 20 R. Ferrando, *J. Phys.: Condens. Matter*, 2015, **27**, 013003.
- 21 D. Bochicchio and R. Ferrando, *Nano Lett.*, 2010, **10**, 4211-4216.
- 22 S. Núñez and R. L. Johnston, *J. Phys. Chem. C*, 2010, **114**, 13255-13266.
- 23 I. Atanasov, R. Ferrando and R. L. Johnston, *J. Phys.: Condens. Matter*, 2014, **26**, 275301.
- 24 A. Shiriyani, M. Wautelet and Y. Belogorodsky, *J. Phys.: Condens. Matter*, 2006, **18**, 2537-2551.
- 25 R. Vallée, M. Wautelet, J. P. Dauchot and M. Hecq, *Nanotechnology*, 2001, **12**, 68-74.
- 26 A. I. Ayesh, S. Thaker, N. Qamhie and H. J. Ghamlouche, *J. Nanopart. Res.*, 2011, **13**, 1125-1131.
- 27 M. Benelmekki, M. Bohra, J.-H. Kim, R. E. Diaz, J. Vernieres, P. Grammatikopoulos and M. Sowwan, *Nanoscale*, 2014, **6**, 3532-3535.
- 28 G. E. Johnson, R. Colby and J. Laskin, *Nanoscale*, 2015, **7**, 3491.
- 29 I. M. L. Billas, A. Châtelain and W. A. de Heer, *Science*, 1994, **265**, 1682-1684.
- 30 E. Quesnel, E. Pauliac-Vaujour and V. Muffato, *J. Appl. Phys.*, 2010, **107**, 054309.
- 31 J. Zhao, E. Baibuz, J. Vernieres, P. Grammatikopoulos, V. Jansson, M. Nagel, S. Steinhauer, M. Sowwan, A. Kuronen, K. Nordlund and F. Djurabekova, *ACS Nano*, 2016, DOI: 10.1021/acs.nano.6b1024.
- 32 F. Yin, Z. W. Wang and R. E. Palmer, *J. Exp. Nanosci.*, 2012, **7**, 703-710.
- 33 A. Elsukova, Z.-A. Li, C. Möller, M. Spasova, M. Acet, M. Farle, M. Kawasaki, P. Ercius and T. Duden, *Phys. Status Solidi*, 2011, **208**, 2437-2442.
- 34 A. Rapallo, G. Rossi, R. Ferrando, A. Fortunelli, B. C. Curley, L. D. Lloyd, G. M. Tarbuck and R. L. Johnston, *J. Chem. Phys.*, 2005, **122**, 194308.
- 35 F. Baletto, C. Mottet and R. Ferrando, *Phys. Rev. B*, 2002, **66**, 155420.
- 36 P. Grammatikopoulos, E. Toulkeridou, K. Nordlund and M. Sowwan, *Modelling Simul. Mater. Sci. Eng.*, 2015, **23**, 015008.
- 37 P. Grammatikopoulos, C. Cassidy, V. Singh and M. Sowwan, *Sci. Rep.*, 2014, **4**, 5779.

- 38 P. Grammatikopoulos, C. Cassidy, V. Singh, M. Benelmekki and M. Sowwan, *J. Mater. Sci.*, 2014, **49**, 3890-3897.
- 39 H. Zhu and R. S. Averback, *Phil. Mag. Lett.*, 1996, **73**, 27-33.
- 40 M. L. Eggersdorfer, D. Kadau, H. J. Herrmann and S. E. Pratsinis, *J. Aerosol. Sci.*, 2012, **46**, 7-19.
- 41 S. Arcidiacono, N. R. Bieri, D. Poulikakos and C. P. Grigoropoulos, *Int. J. Multiphas. Flow*, 2004, **30**, 979-994.
- 42 S. J. Zhao, S. Q. Wang and H. Q. Ye, *J. Phys.: Condens. Matter*, 2001, **13**, 8061-8069.
- 43 H. H. Kart, G. Wang, I. Karaman and T. Çağın, *Int. J. Mod. Phys. C*, 2009, **2**, 179-196.
- 44 F. Ding, A. Rosén and K. Bolton, *Phys. Rev. B*, 2004, **70**, 075416.
- 45 M. M. Mariscal, S. A. Dassie and E. P. M. Leiva, *J. Chem. Phys.*, 2005, **123**, 184505.
- 46 M. Chandross, *Modelling Simul. Mater. Sci. Eng.*, 2014, **22**, 075012.
- 47 L. Martínez, M. Díaz, E. Román, M. Ruano, D. Llamosa P. and Y. Huttel, *Langmuir*, 2012, **28**, 11241-11249.
- 48 M. Benelmekki, J. Vernieres, J.-H. Kim, R. E. Diaz, P. Grammatikopoulos and M. Sowwan, *Mater. Chem. Phys.*, 2015, **151**, 275-281.
- 49 M. Bohra, V. Singh, M. Sowwan, J.-F. Bobo, C.-J. Chung and B. Clemens, *J. Phys. D: Appl. Phys.*, 2014, **47**, 305002.
- 50 J. Alonso, M. L. Fdez-Gubieda, G. Sarmiento, J. Chaboy, R. Boada, A. García Prieto, D. Haskel, M. A. Laguna-Marco, J. C. Lang, C. Meneghini, L. Fernández Barquín, T. Neisius and I Orue, *Nanotechnology*, 2012, **23**, 025705.
- 51 H. Haberland, M. Mall, M. Moseler, Y. Qiang, T. Reiners and Y. Thurner, *J. Vac. Sci. Technol. A*, 1994, **12**, 2925-2930.
- 52 S. Plimpton, *Journal of Computational Physics*, 1995, **117**, 1-19.
- 53 P. L. Williams, Y. Mishin and J. C. Hamilton, *Modelling Simul. Mater. Sci. Eng.*, 2006, **14**, 817-833.
- 54 S. Nosé, *J. Chem. Phys.*, 1984, **81**, 511-519.
- 55 W. G. Hoover, *Phys. Rev. A*, 1985, **31**, 1695-1697.
- 56 V. Singh, P. Grammatikopoulos, C. Cassidy, M. Benelmekki, M. Bohra, Z. Hawash, K. W. Baughman and M. Sowwan, *J. Nanopart. Res.*, 2014, **16**, 2373.
- 57 M. A. Koten, P. Mukherjee and J. E. Shield, *Part. Part. Syst. Charact.*, 2015, **32**, 848-853.
- 58 B. Aufray, M. Göthelid, J.-M. Gay, C. Mottet, E. Landemark, G. Falkenberg, L. Lottermoser, L. Seehofer and R. L. Johnson, *Microsc. Microanal. Microstruct.*, 1997, **8**, 167.
- 59 L. Vitos, A. V. Ruban, H. L. Skriver and J. Kollár, *Surf. Sci.*, 1998, **411**, 186.
- 60 S. S. Hayat, M. A. Ortigoza, M. A. Choudry and T. S. Rahman, *Phys. Rev. B*, 2010, **82**, 085405.
- 61 H. Yildirim and T. S. Rahman, *Phys. Rev. B*, 2009, **80**, 235413.

- 62 H. Sbiaai, Y. Boughaleb, J.-Y. Raty, A. Hajjaji, M. Mazroui and A. Kara, *J. Optoelectron. Adv. M.*, 2012, **14**, 1059-1065.
- 63 P. Lu, M. Chandross, T. J. Boyle, B. G. Clark and P. Vianco, *APL Materials*, 2014, **2**, 022107.
- 64 Y. W. Lee and H. I. Aaronson, *Acta Metall.*, 1980, **28**, 539.
- 65 D. Bochicchio and R. Ferrando, *Eur. Phys. J. D*, 2012, **66**, 115.
- 66 J. Chen, B. Wiley, Z.-Y. Li, D. Campbell, F. Saeki, H. Cang, L. Au, J. Lee, X. Li and Y. Xia, *Adv. Mater.*, 2005, **17**, 2255-2261.

#### Supplementary Material

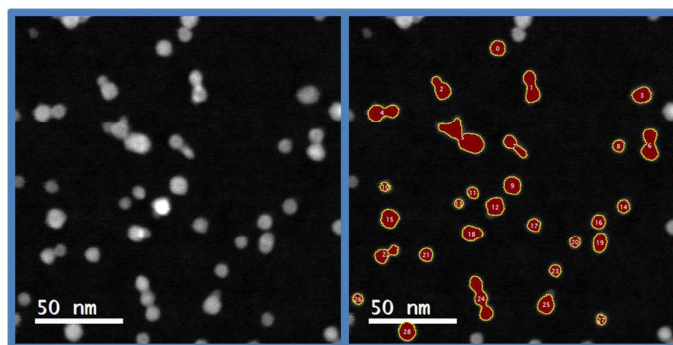


**Fig. S1** Example of identification of observed entities considered to be a single NP (Ag-rich sample).

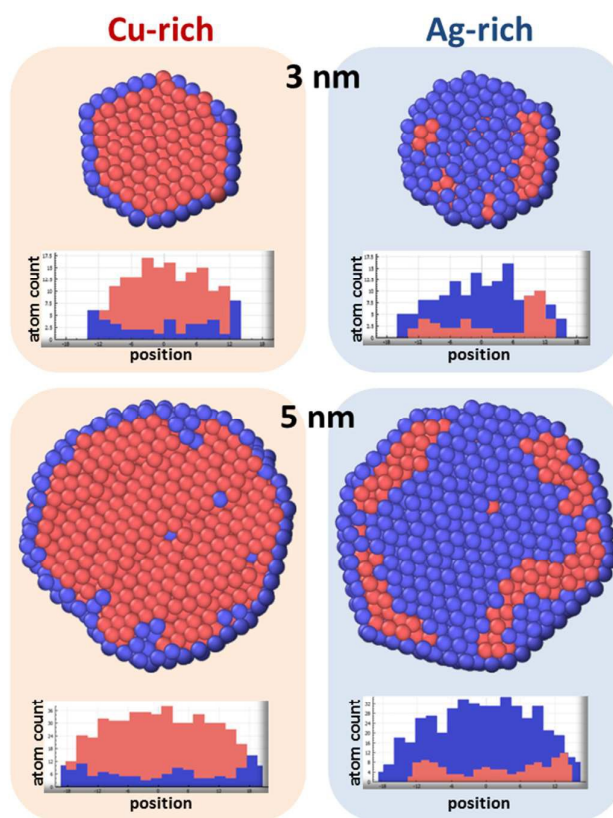


**Fig. S2** Cross-sections of Cu-rich and Ag-rich nanoparticles, 3 and 5 nm in diameter after annealing at 700 K, obtained by combined MD and MC simulation runs of  $\sim 10$  ns and  $\sim 2 \times 10^6$  MC steps, respectively. Red and blue spheres represent Cu and Ag atoms, respectively. Similarly to the pure MD results, a clear tendency for formation of Cu@Ag core/shell structures is observed in the Cu-rich cases, whereas Ag@Cu@Ag onion-type structures emerge in the Ag-rich shapes. The histograms in the bottom of all figures show the populations of each atomic species across the equatorial plane of the particles, verifying these structures. NP sizes are to scale.

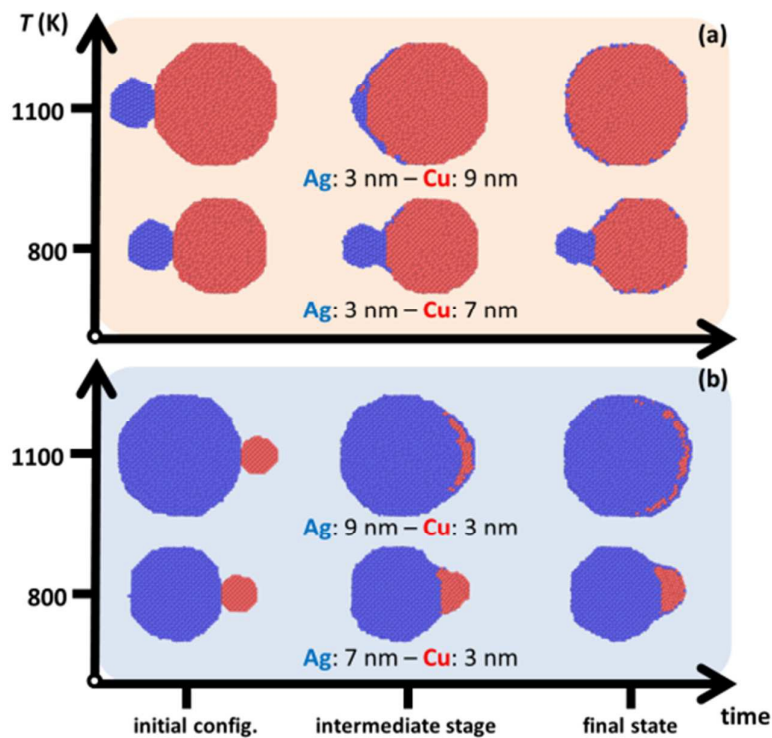


**Fig. S3** Equatorial cross-sections of both (a) Cu-rich and (b) Ag-rich systems, demonstrating the evolution of the coalescence process. At 800 K, relatively enhanced coalescence can be observed after  $\sim 180$  ns. At 1100 K, both systems reach a stable configuration, similar to those of Fig. 5, much faster (after  $\sim 35$  ns).